A Touch-Communication Framework for Drug Delivery Based on a Transient Microbot System

Yifan Chen, Panagiotis Kosmas, Putri Santi Anwar, and Limin Huang

Abstract

Recent progress in bioresorbable radio frequency electronics and engineered bacteria has promised the prospect of realizing transient microbot systems (TMS) for therapeutic applications. The inorganic or organic miniature robots will dissolve into the human body after completing the required tasks and cause no side-effect. In this paper, we propose a potential architecture of TMS for transporting a pharmaceutical compound inside the body, and analyze the system using a micro-to-macro cross-scale communication model. The remote controllability and tangibility of TMS essentially lead to a "touch-communications" (TouchCom) paradigm. The externally maneuverable and trackable TMS are responsible for the delivery of drug particles (*information molecules* in the TouchCom context). The loading/injection and unloading of the drug correspond to the *transmitting* and *receiving* processes in the TouchCom framework. Subsequently, we investigate simulation tools for the propagation and transient characteristics of TMS in the blood vessels. We also define the propagation delay, path loss, as well as angular and delay spectra of targeting intensity, which are parallel to their counterpart concepts in the conventional wireless channel. Finally, our approach is illustrated with comprehensive simulation studies of targeted drug delivery by using the proposed analytical framework integrating robotics and communications at crossover lengthscales.

Index Terms

Transient microbot systems (TMS), touch communications (TouchCom), micro-to-macro cross-scale communication model, bioresorbable electronics, biodegradable bacteria, targeted drug delivery

Y. Chen is with the Department of Electrical and Electronic Engineering, South University of Science and Technology of China, Shenzhen, China (e-mail: chen.yf@sustc.edu.cn).

P. Kosmas is with the School of Natural and Mathematical Sciences, King's College London, London, UK.

P. S. Anwar and L. Huang are with the Department of Chemistry, South University of Science and Technology of China, Shenzhen, China.

I. Introduction

A. Background and Motivation

In his seminal lecture "There's Plenty of Room at the Bottom" in 1959 [1], Feynman presented the revolutionary idea of building tiny, swallowable robots for medical applications. The talk laid the conceptual foundations for the micro/nanorobotics. The recent development of active semiconductors exhibiting transient behavior [2], [3] can revolutionize research in microbotics. These systems offer remarkable levels of functionalities and can physically disappear at prescribed times and at controlled rates [3]. Furthermore, latest advances in biorobotics have promised the prospect of realizing flagellated magnetotactic bacteria (MTB). The MTB are biodegradable and their lifespan is dependent on the micro-environmental conditions such as the temperature of blood and the width of vasculature, which is beneficial from the perspective of biocompatibility and safe *in vivo* operations. By combining the concepts of miniature robots and degradable electronics/engineered bacteria, we can envisage transient microbot systems (TMS), which are remotely controllable and biologically resorbable [4].

Targeted drug delivery aims at delivering a therapeutic agent or drug where medication is needed without affecting other healthy parts of the human body [5]. This process can be viewed as a molecular communication system that uses principles beyond classical electromagnetism [6]–[17]. An engineered miniature transmitter releases small particles (information molecules through which messages are encoded) into a fluid propagation medium. The particles propagate by applying either passive (e.g., diffusion) or active (e.g., with molecular motors) transport schemes, and are eventually received at a miniature receiver, where messages are decoded. Under this framework, the drug particles are information carriers, which deliver messages (healing actions) from the transmitter location (injection site) to the receiver location (targeted site).

By integrating robotics and communications "at the bottom", this work presents a TMS-assisted micro-to-macro cross-scale communication model as an abstraction of targeted drug delivery in the human body. Macroscopically maneuverable and trackable TMS are employed as the vehicles carrying drug particles (i.e., *information molecules*). The TMS exist for medically useful time frames before gradually dissolving into biofluids via resorption by the body, and their pathway represents the *channel* for information exchange, and. The loading/injection and unloading of the therapeutic agent correspond to the *transmitting* and *receiving* processes in the context of information exchange. In this way, a novel paradigm of *touch communications* (TouchCom) is achieved, which provides a visual display of information flow such that the external macro-unit (MAU) can control the movement of TMS by "touching" the tangible TMS-

manoeuvring space with a guiding force.

The TMS-assisted TouchCom has the potential to simplify the requirements of previous molecular communication models by taking into account that: (i) micro/nanomachines cannot process complex information, perform heavy computation, or store large amounts of data; (ii) micro/nanomachines cannot modify freely molecules or control accurately the molecule release/reception process for message encoding/decoding; and (iii) there is no effective mechanism to account for uncertainties during the propagation process, which can be caused by various mechanisms such as random Brownian motions, irregular change of temperature or pH value, unexpected chemical reactions in the fluid environment, random decomposition or degeneration of molecules, etc. By moving most operations to the MAU, the TouchCom process only demands the simplest functionalities (sensing and manoeuvring) at the TMS. Moreover, remote controllability and trackability of the TMS reduce propagation delay and environmental uncertainty.

B. Main Contributions

The main contributions of the current work can be summarized as follows.

1) We propose a cross-scale system architecture to facilitate communications. Specifically, we present the constituent elements of TMS and discuss the fundamental methodology used for information transfer by establishing the useful analogy between the TouchCom and drug delivery. Subsequently, we propose a novel channel description framework for the TouchCom by defining the quantities of propagation delay, path loss, as well as angular and delay spectra of signal strength (i.e., amount of drug delivered to the targeted site), which are parallel to their counterpart concepts in the traditional wireless channel.
2) We propose simulation tools for the propagation and transient characteristics of a TMS swarm in the blood vessels. The former is modeled using a fractal-based random walk process and the latter is divided into three different components due to three different phenomena: diffusion, branching, and degeneration.
3) We present the paradigm of TouchCom by applying the principle of "*seeing-is-communicating*" to visualize the entire process of information transfer in real time. Consequently, we can adjust adaptively the next movement of the TMS swarm "on the fly" based upon the previous observation on the past trajectory of the swarm. Eventually, we propose a cognitive control engine to optimize the performance of the TouchCom.

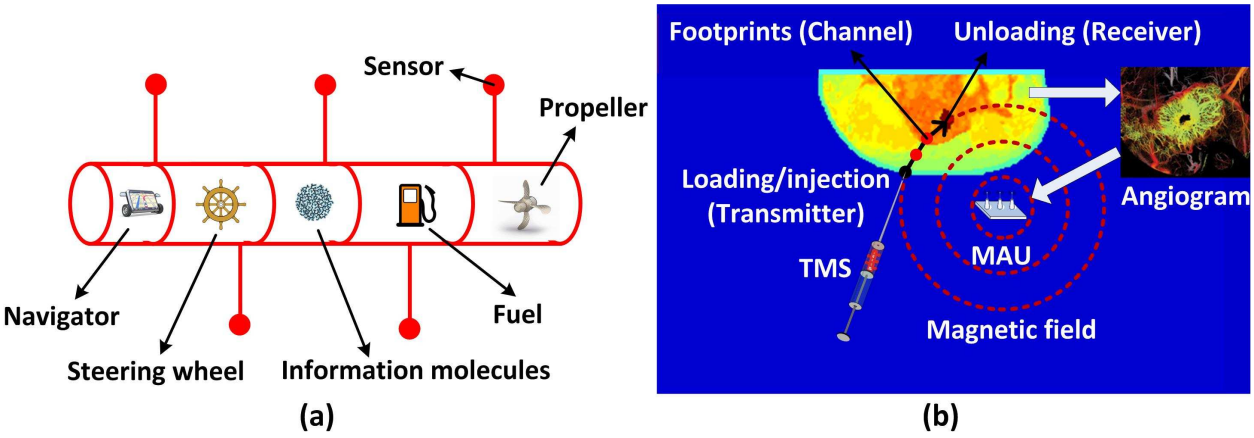

Fig. 1. (a) Key functional elements of a TMS and (b) conceptual illustration of the TMS-oriented TouchCom model for targeted drug delivery.

C. Organization of the Paper

The paper is organized as follows. In Sections II, we present the architecture of the proposed TMS-oriented small-scale communications by establishing the analogy between the TouchCom and targeted drug delivery. We then introduce various parameters to describe the TouchCom channel with this analogy in mind. In Section III, we analyze the simulation tools to describe the movement and transient characteristics of the TMS swarm, as well as the loading/unloading operations. In Section IV, we look into cognitive design strategies for the proposed system. Finally, Section V provides comprehensive simulation studies of targeted drug delivery to demonstrate the principles of the analytical framework, with conclusions provided in Section VI.

II. TMS-ORIENTED TOUCHCOM

A. TMS Model Motivated by Experimental Findings

Water soluble and biocompatible constituent materials such as silicon nanomembranes, silicon dioxide or magnesium oxide, and silk [2] have been used to manufacture radio frequency components such as antennas, rectifying diodes, transistors, capacitors, inductors, resistors, ring oscillators, etc. Subsequently, transient devices offering remarkable levels of functionalities such as sensors, actuators, power supplies, and energy harvesting sub-systems have been achieved [3]. In addition, locomotiveness demanded in a TMS can be accomplished with the manipulation of Lorentz forces on current-carrying wires based on magnetohydrodynamics, or on asymmetries in fluid drag forces experienced by an oscillating structure

TABLE I

ONE-TO-ONE CORRESPONDENCE BETWEEN TMS AND TRANSIENT ELECTRONICS OR MTB

TMS	Transient Electronics	MTB
Propeller	Lorentz forces	Flagellar bundles
Sensor	Nanocircuit biosensors	Receptor channels
Fuel	Wireless power scavenger	Nutrients-to-protons converter
Information molecules	Nanocomposites	Nanocomposites
Steering wheel	Magnetohydrodynamics/asymmetric fluid drag steering	Chains of magnetosomes
Navigator	Passive or active positioning	Passive or active positioning

[18]. The current technology can achieve mm-sized devices. Further miniaturization of various building blocks can be realized with advancements in the fabrication processes and the constituent materials. In addition to silicon-based systems, bacteria-based systems such as the biodegradable flagellated MTB developed by Martel *et al.* [19]–[24] are also considered as possible TMS for our TouchCom paradigm. The use of an MTB as a TMS has been discussed in our previous works [25], [26].

Nanocomposites can be loaded onto the TMS by utilizing biological or chemical bounding methods [8]. The nanocomposites can also be functionalized by means of proper molecular groups such as peptides or antibodies, which are able to bind to receptors at the unloading destination [8]. In order to deliver sufficient amount of nanocomposites to a destination, a swarm of TMS can be injected simultaneously [19], [20].

Based on these experimental findings, we have developed a conceptual model of a TMS [25], [26], which comprises the functional elements depicted in Fig. 1(a) and listed in Table 1. It is worth noting that, the navigator is implemented at the TMS, but the tracking operation is performed at the MAU, as detailed in the next section. Either active or passive methods can be employed for navigation. In the former case, information molecules could be labeled with fluorescent carbon nanotubes or quantum dots. This procedure enables the nanocomposites to feed the location of the TMS swarm directly back to the MAU [27], [28]. In the latter case, information molecules in the form of a microwave contrast agent such as carbon nanotubes or ferroelectric nanoparticles can be employed. The nanocomposites do not provide the position of the swarm explicitly. Instead, the MAU performs differential microwave imaging to localize the swarm [25], [29]. The one-to-one correspondence between the TMS and the transient electronics or MTB is illustrated in Table I.

B. System Architecture of TouchCom

We illustrate the TMS-based TouchCom model for drug delivery in Fig. 1(b), where the information molecules are theranostic agents. Nevertheless, the general framework is applicable to other user scenarios such as monitoring and control of food and water qualities, NBC (nuclear, biological and chemical) conditions, environmental pollution, etc. The loading/injection process is the binding of drug particles to the TMS and the introduction of the TMS in the vascular network at a predefined injection site. We abstract the loading/injection operation as the TouchCom transmitting process with $S_T\delta(t)$ being the transmitted signal, where S_T is the number of injected particles attached to the TMS and $\delta(t)$ is the Dirac delta function.

As illustrated in Fig. 1(b), the MAU can apply angiography to visualize partially the inside, or lumen, of blood vessels in the human organ under examination and treatment. Current medical technologies can achieve 0.3 mm resolution with the volume CT and less than 100 $\mu\mathrm{m}$ with the micro-CT [30]. The MAU generates a magnetic field, and the TMS sense this field and move towards its gradient. While continuous tracking of TMS could be achieved for active navigation mode, our approach is based on defining intermediate aggregation zones (AZs), where the TMS are gathered to reduce diffusion and branching losses.

Under passive navigation mode, the position of a TMS swarm is estimated upon arrival in an AZ, resulting in "footprints" observed at the MAU. These are shown as circular red regions in Fig. 1(b). During traveling to the AZs, the TMS swim at different velocities and as such they disperse, making the density too low for tracking [19], [20]. Let's consider, for example, the MTB studied in [19], [20], [25]. A relatively weak magnetic field is generated towards an AZ, whose size can typically be in the millimeter range. Assume that the boundary of the AZ corresponds to approximately 0.5 Gauss of magnetic field, with the center at 0 Gauss. When outside the AZ, the MTB follow the line of magnetic field. When inside the zone, the MTB are no longer influenced by magnetotaxis and begin random motions. If the MTB exit the AZ, the magnetic field forces them to move back to the zone by magnetotaxis. We abstract the propagation process [TMS footprints as shown in Fig. 1(b)] as the TouchCom channel, where the transmitted signal is sent via the active transport scheme.

When the TMS reach the destination, the drug particles (information molecules) will be removed from the vehicles and get assimilated into the targeted site allowing them to perform healing actions. As the theranostic agent assists in the tracking operation, its binding to the targeted site deactivates the navigator component. Subsequently, the location where the drug particles finally accumulate will give rise to a "sink"

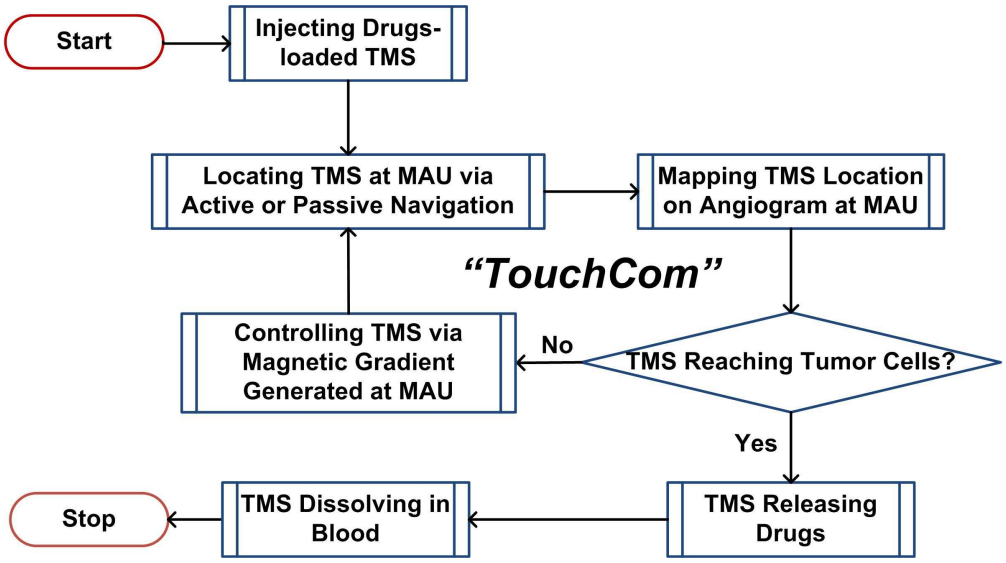

Fig. 2. Operation procedure of the proposed system.

on the visual display of the TMS propagation route. As the TMS are made of biodegradable electronics or bacteria, they will dissolve in the blood after completing their tasks. We abstract the unloading operation as the TouchCom receiving process with $S_R\delta(t-\tau)$ being the received signal, where S_R is the number of particles successfully discharged at the targeted site and τ is the propagation delay.

In summary, the main operations of TMS only involve propulsion and steering, which are achievable with the current micro/nanobotic technologies. On the other hand, the complex operations of TMS controlling and positioning are performed at the macroscopic MAU. Furthermore, the small-scale communication process is facilitated through a micro-to-macro system architecture. The operation procedure of the whole system is illustrated in Fig. 2. Note that the loop incorporating both controlling and tracking steps underlies the TouchCom principle to be elaborated in Section IV.

C. Description Methods for the TouchCom Channel

Structures of human vascular systems have been widely described using complex geometrical (fractal) models according to principles of optimal network formation [31], [32]. The whole vascular tree is approximated by a dichotomously branching system of tubes known as bifurcation as illustrated in Fig. 3. More details on the model of vasculature will be discussed in Section III-A. The signal observed at the receiver has a random amplitude, delay, and angle due to the irregular vasculature. The directional impulse response widely used in describing traditional wireless channels can be applied to the TouchCom

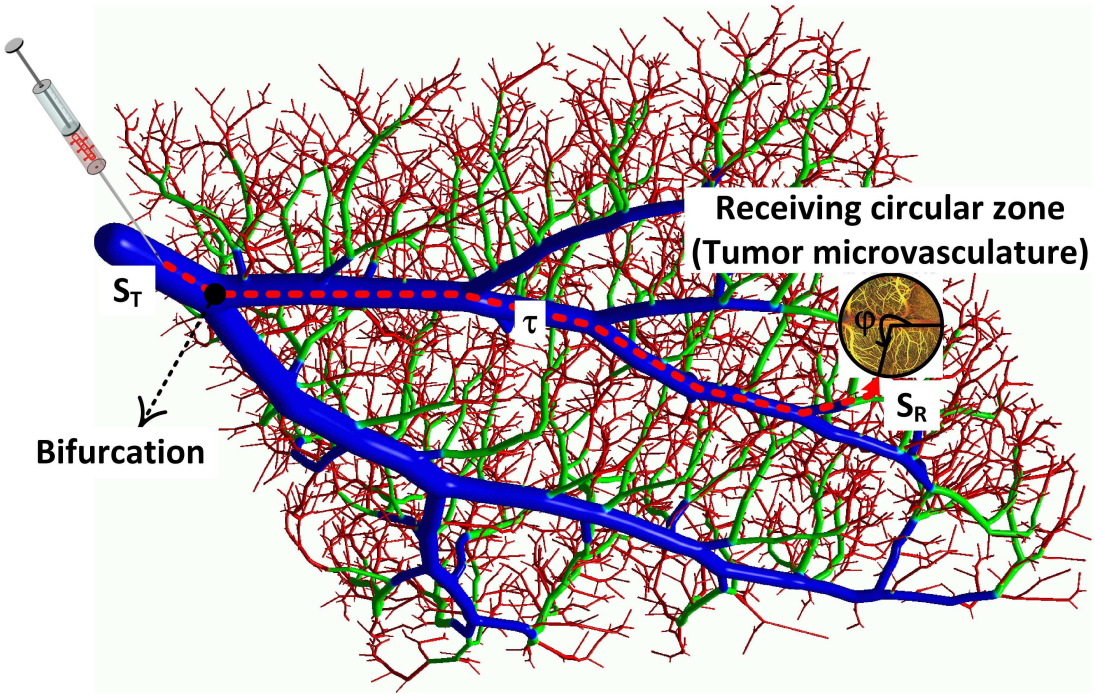

Fig. 3. Propagation of TMS in the vascular tree and definitions of TouchCom channel parameters. The vascular tree is formed of multiple bifurcating branches.

channel. Nevertheless, while traditional channels often exhibit multipath phenomena, the TouchCom channel comprises only a single path, which can be expressed as

$$h(\tau, \varphi) = h_0 \delta(\tau - \tau_0)\, \delta(\varphi - \varphi_0)\,. \tag{1}$$

According to this model, the impulse response depends on three random variables, the path loss $h_0 = S_R/S_T$, the delay τ_0 and the azimuth φ_0. As illustrated in Fig. 3, we define a receiving circular zone, representing the tumor microenvironment (microvasculature). The path loss h_0 is caused by three different signal attenuation mechanisms, namely, diffusion, branching, and degeneration, which can occur during propagation of TMS from the injection site to the boundary of the receiving zone. The delay τ depends on the propagation route and the speed of TMS. Finally, the azimuth φ is defined as the angle-of-arrival at the receiving zone as depicted in Fig. 3.

As in the analysis of wireless channels, we can develop a spatial-temporal description of TouchCom channels. The most fundamental quantity is the delay-azimuth spectrum, computed by averaging over all

impulse responses:

$$\Xi_{\tau,\varphi}(\tau,\varphi)=\alpha\mathbb{E}\left\{h\middle|\tau,\varphi\right\}f_{\tau,\varphi}(\tau,\varphi)=\alpha\mathbb{E}\left\{h_0\middle|\tau_0=\tau,\varphi_0=\varphi\right\}f_{\tau,\varphi}(\tau,\varphi), \tag{2}$$

where $\mathbb{E}\{\cdot\}$ denotes the expectation operator. The normalization factor α ensures that $\Xi_{\tau,\varphi}(\tau,\varphi)$ is a probability density function (pdf).

Following (2), the TouchCom channel azimuth spectrum and delay spectrum are derived as

$$\Xi_{\varphi}(\varphi)=\int_{\tau}\Xi_{\tau,\varphi}(\tau,\varphi)\mathrm{d}\tau=\int_{\tau}\alpha\mathbb{E}\left\{h_0\middle|\tau_0=\tau,\varphi_0=\varphi\right\}f_{\tau,\varphi}(\tau,\varphi)\mathrm{d}\tau, \tag{3}$$

$$\Xi_{\tau}(\tau)=\int_{\tau}\Xi_{\tau,\varphi}(\tau,\varphi)\mathrm{d}\varphi=\int_{\varphi}\alpha\mathbb{E}\left\{h_0\middle|\tau_0=\tau,\varphi_0=\varphi\right\}f_{\tau,\varphi}(\tau,\varphi)\mathrm{d}\varphi. \tag{4}$$

The formulations apply to the ensemble average of many spatial realizations of the vascular network, such that the descriptions can be expressed as a continuous spectrum. The parameters in (3) and (4) are parallel to the definitions of power azimuth spectrum and power delay spectrum in classical wireless channels [33], [34].

We can also apply different ways to characterize the amount of TouchCom signal dispersion in the spatial domain, which measures the width of azimuth spectrum. One approach follows the classical definition in [34]:

$$\sigma_{\varphi}=\sqrt{\int_{\varphi}\left|\exp(j\varphi)-\mu_{\varphi}\right|^2\Xi_{\varphi}(\varphi)\mathrm{d}\varphi}, \tag{5}$$

where

$$\mu_{\varphi}=\int_{\varphi}\exp(j\varphi)\Xi_{\varphi}(\varphi)\mathrm{d}\varphi. \tag{6}$$

Alternatively, if the azimuth spectrum has a symmetric shape with respect to the line-of-sight direction ($\varphi=0^{\circ}$), the angular spread can be defined as

$$\sigma_{\varphi}=\sup\left\{\hat{\varphi}\in[0,\varphi_{\max}]:\int_{-\hat{\varphi}}^{\hat{\varphi}}\Xi_{\varphi}(\varphi)\mathrm{d}\varphi<\epsilon\right\}, \tag{7}$$

where $\varphi_{\max}$ is the maximum azimuth. This parameter defines the supremum limit of angular extent, within which the percentage of received signal strength as compared to the total strength is less than a sufficiently large value ϵ.

Suppose that the delay spectrum is a non-increasing function due to the increased path loss with delay. The delay spread can be defined in a similar way to (7):

$$\sigma_{\tau}=\sup\left\{\hat{\tau}\in[\tau_{\min},\tau_{\max}]:\int_{-\hat{\tau}}^{\hat{\tau}}\Xi_{\tau}(\tau)\mathrm{d}\tau<\epsilon\right\}, \tag{8}$$

where $\tau_{\min}$ and $\tau_{\max}$ are the minimum and maximum delays.

III. Simulation Models

We present simulation models of the movement and transient characteristics of a TMS swarm in vasculature. We first look into the scenario when the blood vessels are resolvable on the angiogram. In the last part of this section, we will describe the models when the blood vessels are angiographically unresolvable.

A. Movement of TMS Swarm in Vasculature

In order to synthesize the movement of a TMS swarm in the blood vessels, a model to characterize the vascular network should be constructed. Vasculature in the human body has two basic functions [31]. Firstly, the distributive function is to bring a stream of blood to every living cell within the body or organ and is achieved by successive dichotomous division, or bifurcation. The self-similarity of bifurcation at each node gives the vascular connection a fractal character. Secondly, the hemodynamic function is to increase the cross-sectional area available to the blood flow in order to bring its velocity down to a level sufficiently low to permit the exchange of metabolic products across the capillary wall. This function governs the relationship between the diameter of the parent vessel and the diameters of two daughter vessels at each node, which follows the generalized Murray's law [31], [32]:

$$d_P^{\beta} = d_{D,1}^{\beta} + d_{D,2}^{\beta}, \tag{9}$$

where subscript P indicates the parent segment and subscripts $D,1$ and $D,2$ indicate the two daughter segments at the same bifurcation. The exponent β is called the bifurcation exponent, which ranges from 2.0 to 3.0 and determines the fractal dimension of a vascular tree. According to [32], β is equal to $2.6 \sim 2.7$ for the human arterial vessels. For large arteries of systemic circulation β is around 2.33. For capillaries β is near 3. The vessel length is proportional to its diameter:

$$L = Kd, \tag{10}$$

where K is a constant for given vessels. For small arteries or capillaries $K \approx 60$.

Vascular bifurcations often exhibit asymmetric structure such that the two branch diameters differ from one junction to the other. Define the ratio of the two diameters

$$\lambda = \frac{d_{D,2}}{d_{D,1}}, \quad d_{D,2} \leq d_{D,1}. \tag{11}$$

For arterial vessels λ is in the range of $0.59 \sim 0.83$ [32]. Substituting (11) into (9) yields

$$\frac{d_{D,1}}{d_P} = \frac{1}{(1+\lambda^{\beta})^{1/\beta}}, \ \frac{d_{D,2}}{d_P} = \frac{\lambda}{(1+\lambda^{\beta})^{1/\beta}}. \tag{12}$$

The self-similarity fractal dimension, $\mathcal{D}_F$, is defined as [31]

$$\mathcal{D}_F = \frac{\ln 2}{\ln 2 - \ln\left(1+\lambda^2\right) + \ln\left(1+\lambda^\beta\right)^{2/\beta}}. \tag{13}$$

Murray's formula also describe the angle between two daughter vessels. Define $\theta_{D,1}$ and $\theta_{D,2}$ to be the angles between daughter branch 1 and the parent segment, and daughter branch 2 and the parent. The following relationships can be obtained [32]:

$$\cos\theta_{D,1} = \frac{d_P^4 + d_{D,1}^4 - d_{D,2}^4}{\left(2d_P d_{D,1}\right)^2}, \quad \cos\theta_{D,2} = \frac{d_P^4 + d_{D,2}^4 - d_{D,1}^4}{\left(2d_P d_{D,1}\right)^2}. \tag{14}$$

The total branch angle $\theta_{D,1} + \theta_{D,2}$ between two daughter vessels after division is known as bifurcation angle, which ranges between 75° and 90°. The minimum angle 75° is obtained when the two daughter branches are equal. Arterial branching angle falls roughly in the range of $60^\circ \sim 80^\circ$. For capillaries this angle is between 80° and 90°.

Real-life physiological data exhibit a large amount of scatter in the values of vessel diameters or in the values of bifurcation exponent [31]. This wide variability in branching data should be incorporated in the simulation studies. Furthermore, as some capillaries are so slender that they can hardly be imaged, the resolvable and unresolvable segments in the vascular network should be identified to represent a realistic angiogram.

Based on the fractal character of vascular branching, we propose a random walk process on the vascular tree as the baseline model for simulating the propagation of a TMS swarm. The algorithm involves the following steps.

1) Let $\mathbf{q}_0 = (x_0, y_0)$ represent the initial position of the swarm, which is determined by the injection site and is assumed to be located on a root vessel with diameter $d_{P,0}$ and length $L_{P,0}$. The initial direction is chosen to be aligned with the root vessel at $\mathbf{q}_0$. Generate a random bifurcation exponent β_0 and a random asymmetry ratio λ_0, which are uniformly distributed in the intervals I_β and I_λ, respectively. These two intervals are dependent on the type of blood vessel. Let $v(t)$ represent the time-varying speed of the swarm, which depends on the propelling mechanism, the blood velocity, and the blood pressure. Let $i = 1$.
2) At the ith bifurcation, calculate the diameters of two daughter segments, $d_{D,i,1}$ and $d_{D,i,2}$, by substituting $d_{P,i-1}$, β_{i-1}, and λ_{i-1} into (12). Calculate two junction branch angles $\theta_{i,1}$ and $\theta_{i,2}$, by substituting $d_{P,i-1}$, $d_{D,i,1}$ and $d_{D,i,2}$ into (14). Generate a binary random number $Z_i \in \{0, 1\}$ that determines the branching direction (i.e., which of the two asymmetrical branches generated at the ith bifurcation level has a larger diameter).

3) At the ith bifurcation, generate a random vessel length $L_{D,i,1}$, which has an exponential distribution of mean $Kd_{D,i,1}$ [see also (10)]:

$$f_{L_{D,i,1}}(L_{D,i,1}) = \frac{1}{Kd_{D,i,1}} \exp\left(-\frac{L_{D,i,1}}{Kd_{D,i,1}}\right). \tag{15}$$

Similarly, generate another exponentially-distributed vessel length $L_{D,i,2}$ with mean $Kd_{D,i,2}$. Subject to a specific controlling strategy as to be discussed in Section IV, select the jth $(j = 1, 2)$ daughter segment to be the traveling path after the ith bifurcation. Define $d_{P,i} = d_{D,i,j}$ and $L_{P,i} = L_{D,i,j}$. Generate two random variables β_i and λ_i, uniformly distributed in the intervals I_β and I_λ, respectively.

4) Check whether the TMS dissolve into the biofluid medium at the jth $(j = 1, 2)$ branch. If the answer is positive, stop the iteration. Otherwise, go to Step 5.

5) Check whether the jth $(j = 1, 2)$ branch intersects the predefined receiving circular zone (tumor microenvironment). If the answer is positive, record the first intersection point as the arrival position of the swarm and stop the iteration. Otherwise, increment i by 1 and go to Step 2.

B. Transient Characteristics of TMS Swarm

We then consider the characteristic models for the transient kinetics of a TMS swarm, which can be divided into three different components caused by three different mechanisms: diffusion, branching, and degeneration. Each mechanism reduces certain percentage of the effective TMS in the swarm, and the overall transience is characterized by the multiplicative effect of these three components. Similarly, we first consider the situation that the vasculature is angiographically resolvable.

1) Diffusion: Based on experimental findings (see e.g., [20]), we assume that an agglomeration of TMS are controlled like a unified organism to swim in the biofulid medium. The number of TMS for each swarm will be typically large. It is thus convenient to deal with their count or concentration in various volumes of space. The diffusion occurs in a controlled environment in one dimension (i.e., blood vessel). Between the ith and $(i+1)$th bifurcations, suppose that the TMS swarm moves in a blood vessel whose cross-sectional area is $A_{P,i} = \pi d_{P,i}^2/4$ and the inside wall of the vessel is impervious to the TMS. As a coarse approximation, we could quantify the TMS diffusion with respect to the centroid of the swarm by using the result in [35]:

$$U_{i,k}(l,t) = \frac{\eta Q_{i,k}}{A_{P,i}\sqrt{\pi D t}} \exp\left(-\frac{l^2}{4Dt}\right), \tag{16}$$

where $Q_{i,k}$ is the number of TMS at the kth AZ between the ith and $(i+1)$th bifurcations, D is the diffusion coefficient of the biological medium in $\mathrm{m}^2/\mathrm{sec}$, t is the propagation time, l is the distance

between an arbitrary TMS and the centroid of the swarm, and η is a scaling factor accounting for the discrepancy between the realistic propagation scenario in a blood vessel and the ideal case in an infinite tube with a perfect reflecting barrier at the source end of the tube. Assume that there is some threshold density $U^\star$ such that the MAU tracking the swarm responds to concentrations of $U^\star$ and greater. The limit distance of the threshold volume is

$$l^\star_{i,k}(t) = \begin{cases} \sqrt{4Dt \ln \frac{\eta Q_{i,k}}{A_{P,i}U^\star\sqrt{\pi Dt}}} & \text{for } 0 \le t \le \left(\frac{\eta Q_{i,k}}{A_{P,i}U^\star}\right)^2 \frac{1}{\pi D}, \\ 0 & \text{Otherwise.} \end{cases} \tag{17}$$

This distance increases through time to a maximum, $\frac{\eta Q_{i,k}}{A_{P,i}U^\star}\sqrt{\frac{2}{\pi e}}$, at time $\left(\frac{\eta Q_{i,k}}{A_{P,i}U^\star}\right)^2 \frac{1}{\pi De}$, then decreases to zero at which time the concentration is everywhere below threshold. The time of ultimate fade out is $\left(\frac{\eta Q_{i,k}}{A_{P,i}U^\star}\right)^2 \frac{1}{\pi D}$.

Subsequently, when only the diffusion loss is considered, the amount of TMS at the $(k+1)\text{th}$ AZ is obtained as

$$\begin{aligned} Q_{i,k+1} &= \int_{-\min\left\{l^\star_{i,k}(t_{i,k,k+1}),L_{P,i}-\ell_{i,k+1}\right\}}^{\min\left\{l^\star_{i,k}(t_{i,k,k+1}),\ell_{i,k+1}\right\}} A_{P,i}U_{i,k}\left(l, t_{i,k,k+1}\right) \mathrm{d}l \\ &= \int_{-\min\left\{l^\star_{i,k}(t_{i,k,k+1}),L_{P,i}-\ell_{i,k+1}\right\}}^{\min\left\{l^\star_{i,k}(t_{i,k,k+1}),\ell_{i,k+1}\right\}} \frac{\eta Q_{i,k}}{\sqrt{\pi D t_{i,k,k+1}}} \exp\left(-\frac{l^2}{4Dt_{i,k,k+1}}\right) \mathrm{d}l \\ &= \eta Q_{i,k}\left[\mathrm{erf}\left(\frac{\min\left\{l^\star_{i,k}(t_{i,k,k+1}), \ell_{i,k+1}\right\}}{\sqrt{4Dt_{i,k,k+1}}}\right) + \mathrm{erf}\left(\frac{\min\left\{l^\star_{i,k}(t_{i,k,k+1}), L_{P,i}-\ell_{i,k+1}\right\}}{\sqrt{4Dt_{i,k,k+1}}}\right)\right] \end{aligned} \tag{18}$$

where $t_{i,k,k+1}$ is the traveling time from the $k\text{th}$ to $(k+1)\text{th}$ AZ, $\ell_{i,k+1}$ is the distance between the $(k+1)\text{th}$ AZ and the $i\text{th}$ bifurcation, and $\mathrm{erf}(\cdot)$ is the Gauss error function. The superscript diff denotes diffusion.

2) Branching: At the $i\text{th}$ bifurcation (see also Fig. 3), when the parent and daughter blood vessels are visible on the angiogram, an AZ at the entrance of the intended daughter branch can be set up to greatly reduce the branching effect. In this case, we will ignore the branching loss in our simulation studies. On the other hand, if the vessels are undetectable inside the human body due to the limit in sensitivity of the imaging modality used, it is more difficult to maintain the convergence of TMS through a carefully set AZ. One possible remedy is to reduce the distance between two successive AZs. This, however, may not be practical in real-life applications due to constraint on drug delivery time. In the worst case, the ratio of the amount of TMS entering two daughter segments is approximated as $d^2_{D,i,1}/d^2_{D,i,2}$ and the branching attenuation is (assuming that the intended path is the 1st daughter vessel) $\rho_{\min} = d^2_{D,i,1}/\left(d^2_{D,i,1} + d^2_{D,i,2}\right)$.

The actual attenuation ρ ranges between $\rho_{\min}$ and 1 depending on the displacement between neighboring AZs, x. For simplicity, we postulate the following exponential relationship between ρ and x:

$$\rho(x) = (1-\rho_{\min}) \exp\left(-\frac{x}{x_0}\right) + \rho_{\min}. \tag{19}$$

The term x_0 is the rate parameter, which is comparable to the length of the blood vessel.

3) Degeneration: This measure quantifies the effect of bioresorption, which is normalized such that it ranges from 0 (no resorption) to 1 (complete resorption).

Following the experimental findings reported in [2], [3], in terms of a silicon-based TMS, the system exhibits two-stage kinetics in its functional transience. For example, immersion of metal-oxide-semiconductor field-effect transistors formed using silicon nanomembranes, silicon dioxide gate dielectrics, and magnesium electrodes, with encapsulating layers of magnesium oxide and silk, in deionized water for up to ∼90 hours caused small change in key device properties. Significant functional degradation then occurred in a narrow time interval (<3 hours) after this period of stable operation. The encapsulation defines the first time scale, whereas the magnesium electrodes define the second. A similar phenomenon was found in the dissolution behavior of other diode devices [2], [3]. Furthermore, a transient bioresorbable device for thermal therapy was implanted under the skin of a Sprague-Dawley rat. Inductive coupling through the skin generated a localized temperature increase to sterilize and maintain asepsis at the wound site. The functional transience had a time scale of 15 days, which was controlled via the crystallinity of the silk package. After this time, the device quickly disappeared [3].

Consequently, to synthesize the two-stage kinetics as well as random bioresorbing, we model the transient characteristics based on a dual-slope Lévy process:

$$C_k = \begin{cases} \mathbf{1}_{[0,1)}\left(L_{t_k}\left(\Lambda_1\right)\right) L_{t_k}\left(\Lambda_1\right) + \mathbf{1}_{[1,\infty)}\left(L_{t_k}\left(\Lambda_1\right)\right) & \text{if } C_{k-1} \in [0, C^*), \\ \mathbf{1}_{[0,1)}\left(L_{t_k}\left(\Lambda_2\right)\right) L_{t_k}\left(\Lambda_2\right) + \mathbf{1}_{[1,\infty)}\left(L_{t_k}\left(\Lambda_2\right)\right) & \text{if } C_{k-1} \in [C^*, 1), \\ 1 & \text{if } C_{k-1} = 1, \end{cases} \tag{20}$$

where $C_0 = 0$ represents the initial condition at $t_0 = 0$ when the TMS swarm has just been injected without any bioresorption. C_k and t_k $(k = 1, 2, \cdots)$ are the transient characteristic and total duration of immersion, respectively, when the TMS arrive at the kth AZ. $L_{t_k}\left(\Lambda_j\right)(j = 1, 2)$ satisfies the following properties of a Lévy process: (i) $L_0 = 0$ almost surely; (ii) (independence of increments) for any $0 \leq t_1 < t_2 < \cdots < t_k < \infty$, $L_{t_2} - L_{t_1}$, $L_{t_3} - L_{t_2}$, $\cdots$, $L_{t_k} - L_{t_{k-1}}$ are independent; (iii) (stationary increments) for any $s < t$, $L_t - L_s$ is equal in distribution to L_{t-s}; and (iv) (continuity in probability) for any $\epsilon > 0$ and $t \geq 0$ it holds that $\lim_{h \to 0} \Pr\left(|L_{t+h} - L_t|\right) = 0$. We consider the exponential process where the probability distribution of $L_{t_k}(\Lambda_j) - L_{t_{k-1}}(\Lambda_j)$ is an exponential distribution with expected

value $(t_k - t_{k-1})/\Lambda_j$. In the dual-slope Lévy process, $0 < 1/\Lambda_1 \ll 1/\Lambda_2 < \infty$ are the rates of the two-stage bioresorbing process. Note that the degeneration of TMS in the biofluid medium is irreversible and therefore, C_k is a non-decreasing sequence. An indicator function $\mathbf{1}_{\mathbb{A}} : L \to \{0, 1\}$ is defined as

$$\mathbf{1}_{\mathbb{A}}(L) \triangleq \begin{cases} 1 & \text{if } L \in \mathbb{A}, \\ 0 & \text{if } L \notin \mathbb{A}. \end{cases} \tag{21}$$

The indicator terms in (20) switch the value of C_k between L_{t_k} (for $0 \leq L_{t_k} < 1$) and 1 (for $L_{t_k} \geq 1$), where the maximum value of 1 indicates complete bioresorption. Furthermore, the critical point C^* determines the boundary of the two regimes of transient kinetics. Finally, the two parameters $t_F = \Lambda_1 C^*$ and $t_P = \Lambda_1 C^* + \Lambda_2 (1 - C^*)$ are the functional lifespan and physical lifespan of TMS, respectively.

In terms of a bacterial TMS (e.g., MTB), the degeneration process is related to decrease in its terminal velocity. Initial experiments conducted in human blood at 37° showed that the velocity V (in $\mu\mathrm{m/s}$) at a time t (expressed in minutes) after the beginning of operations of the MTB decreased according to [19]

$$V = 0.0907t^2 - 8.0966t + V_0, \tag{22}$$

where V_0 is the initial average velocity of the MTB prior to being injected into blood. The MTB would remain effective for a duration of ~ 40 min, and the decrease in speed was probably caused by the relatively high temperature of blood. The second-order polynomial regression model in (22) is not convenient for simulation studies and theoretical analysis. Instead, we propose to use an exponentially decaying function to approximate the swimming speed of MTB in blood:

$$V(t) = V_0 \exp\left(\frac{t}{t_0}\right), \tag{23}$$

where t_0 determines the decaying rate of speed with respect to time. To approximate the relationship in (22), t_0 is chosen to be around 15 minutes by visual inspection.

The swimming speeds from a large sample of MTB have been measured by Martel *et al.* with a video camera mounted on an optical microscope in reflection-mode microscopy using dark-field illumination [19]. Based on the observation in [19], we could model the terminal velocity distribution of the MTB using a truncated Gaussian pdf with mean $\mu_V = V(t)$ and standard deviation $\sigma_V \approx 60$ $\mu\mathrm{m/s}$ (i.e. without *a priori* selection) or $\sigma_V \approx 20$ $\mu\mathrm{m/s}$ (i.e. with *a priori* selection). As shown in [19], the minimum and maximum speeds are given by $V_{\min} = 0$ $\mu\mathrm{m/s}$ and $V_{\max} = 300$ $\mu\mathrm{m/s}$, respectively. Suppose that the threshold velocity below which an MTB is deemed degenerated is V_{th}. The percentage of effective MTB upon arrival at the $k\mathrm{th}$ AZ, where the total immersion time is t_k, can be calculated as the probability

that the random velocity of an arbitrary MTB, v, is less than $V_{\rm th}$:

$$C_k = \Pr\left(v \le V_{\rm th}\right) = \frac{\operatorname{erf}\left[\frac{V_{\rm th}-V(t_k)}{\sqrt{2\sigma_V^2}}\right] - \operatorname{erf}\left[\frac{V_{\min}-V(t_k)}{\sqrt{2\sigma_V^2}}\right]}{\operatorname{erf}\left[\frac{V_{\max}-V(t_k)}{\sqrt{2\sigma_V^2}}\right] - \operatorname{erf}\left[\frac{V_{\min}-V(t_k)}{\sqrt{2\sigma_V^2}}\right]} \tag{24}$$

C. Derivation of TouchCom Channel Parameters

When the TMS swarm reaches the targeted site, the percentage of drug consumed during the propagation phase (i.e., the path loss) can be derived by accounting for the three transience mechanisms mentioned above:

$$\begin{aligned} h_0 &= \frac{S_R}{S_T} \\ &= \underbrace{\prod_{i=0}^{I}\prod_{k=0}^{K_i}\frac{Q_{i,k+1}}{Q_{i,k}}}_{\text{diffusion}} \times \underbrace{\prod_{i=1}^{I}\rho_i}_{\text{branching}} \times \underbrace{\left(1 - C_{\sum_{i=0}^{I}K_i}\right)}_{\text{degeneration}}, \end{aligned} \tag{25}$$

where I is the total number of bifurcation, K_i is the number of AZs at the ith bifurcation, and the K_Ith AZ is the tumor microvasculature as shown in Fig. 3. $Q_{0,0} = S_T$ denotes the initial number of TMS. Furthermore, $Q_{i,K_i} = Q_{i+1,0}$ for $i = 0, 1, \cdots, I-1$. Substituting (18)-(20) and (24) into (25) yields the overall path loss. The overall delay τ is given by the submission of all propagation delays between consecutive AZs as well as the tracking times at these zones. Furthermore, as illustrated in Fig. 3, the incident angle φ is defined as the angle between the line joining the center of the receiving circular zone (tumor microvasculatre) and the point where the TMS path intersects the receiving zone and the horizontal axis.

D. Simulation Models for Angiographically Unresolvable Vasculature

When the blood vessels are too tiny to be imaged, the vascular network could be approximated as a homogeneous fluid medium. Subsequently, the movement of the TMS swarm can be modeled using a velocity-jump random walk process [4]. We assume that the swarm moves forward with a time-varying speed for a time step of random length, which is governed by a Poisson process with turning frequency ϖ. Hence, the mean run length time is $1/\varpi$. The swarm then changes its direction, with the new direction (angle) generated via the von Mises pdf, which has been commonly employed in the simulation of correlated random walks for the distribution of turning angle at each step [36]. The mean of this pdf depends on the propelling field at the present location of the swarm and thus introduces a directional bias. Our movement simulation algorithm involves the following steps:

1) Let $\hat{\mathbf{q}}_0 = (\hat{x}_0, \hat{y}_0)$ represent the initial position of the swarm, which is determined by the location where it enters the unresolvable zone on the angiogram. The initial direction is chosen to be aligned with the external field at $\hat{\mathbf{q}}_0$. Let $v(t)$ represent the speed of the swarm, ϖ the turning rate, and κ the concentration parameter of the von Mises velocity (direction) jump. Let $i = 0$.
2) Obtain a random time step Δt_i as a result of a Poisson process of intensity ϖ. Consequently, Δt_i follows an exponential distribution of mean $1/\varpi$, with pdf

$$f_{\Delta t_i}(\Delta t_i) = \varpi \exp(-\varpi \Delta t_i). \tag{26}$$

Obtain a random angle $\Delta\theta_i$ from the von Mises distribution of mean 0 and concentration κ, using an envelope-rejection method based on a wrapped Cauchy distribution [37]. The pdf is given by

$$f_{\Delta\theta_i}(\Delta\theta_i) = \frac{1}{2\pi I_0(\kappa)} \exp(\kappa \cos \Delta\theta_i), \tag{27}$$

where I_0 denotes the modified Bessel function of the first kind and order 0. The distribution is unimodal and is symmetrical about 0. The mode is at $\theta = 0$ and the width of the angular spread is controlled by κ. For $\kappa = 0$, the pdf is equal to the uniform distribution; while $\kappa \to \infty$ yields a sharply peaked distribution about 0.
3) Obtain the new position $\hat{\mathbf{q}}_{i+1} = (\hat{x}_{i+1}, \hat{y}_{i+1})$ from the old position $\hat{\mathbf{q}}_i = (\hat{x}_i, \hat{y}_i)$, given Δt_i and $\Delta\theta_i$ generated in Step 2, using the simple trigonometry as follows:

$$\hat{x}_{i+1} = \hat{x}_i + \left[\int_0^{\Delta t_i} v(t;i)\mathrm{d}t\right] \cos(\theta_i + \Delta\theta_i) \tag{28}$$

and

$$\hat{y}_{i+1} = \hat{y}_i + \left[\int_0^{\Delta t_i} v(t;i)\mathrm{d}t\right] \sin(\theta_i + \Delta\theta_i), \tag{29}$$

where θ_i is the angle of the external field at $\hat{\mathbf{q}}_i$.
4) Increment i by 1 and go to Step 2, unless a stopping condition is reached (e.g., the swarm dissolves into the blood or reaches the tumor microenvironment).

The next step is to characterize the transient behavior of the TMS swarm. Firstly, the diffusion and branching effects can be combined into a two-dimensional diffusion process with respect to the centroid of the swarm [35]:

$$U(r,t) = \frac{Q}{4\pi D t} \exp\left(-\frac{r^2}{4Dt}\right), \tag{30}$$

where Q is the amount of TMS at the origin, D is the diffusion coefficient of the biological medium in $\mathrm{m}^2/\mathrm{sec}$, t is the propagation time, and r is the distance between an arbitrary TMS and the centroid of the swarm. Similar to (17), assume that there is some threshold density $U^\star$ such that the MAU tracking

the TMS responds to concentrations of $U^\star$ and greater. The line of concentration of $U^\star$ at time t is a circle with center at the centroid and radius

$$r^\star(t) = \begin{cases} \sqrt{4Dt \ln \frac{Q}{4\pi DtU^\star}} & \text{if } 0 \le t \le \frac{Q}{4\pi DU^\star}, \\ 0 & \text{Otherwise.} \end{cases} \tag{31}$$

Subsequently, the average number of TMS at the kth AZ is obtained as

$$\begin{aligned} Q_k &\approx \int_0^{r^\star(t_k)} 2\pi r U\left(r, t_k\right) \mathrm{d}r \\ &= \int_0^{r^\star(t_k)} \frac{Qr}{2Dt_k} \exp\left(-\frac{r^2}{4Dt_k}\right) \mathrm{d}r \\ &= Q\left\{1 - e^{-\frac{[r^\star(t_k)]^2}{4Dt_k}}\right\} \end{aligned} \tag{32}$$

where t_k is the propagation time from the moment the swarm enters the unresolvable region to the kth AZ in the region. Eq. (32) ignores the TMS diffusion loss outside AZs and assumes that the time spent in traveling from one zone to another is much longer than the time spent at each zone.

In terms of the degeneration loss, the same models as those in (20)-(24) can be applied.

IV. Cognitive Engine for TouchCom

For the proposed TouchCom framework, the external MAU is able to decide partially the propagation path of TMS. On the other hand, the movement of TMS is influenced by the unknown *in vivo* environment under surveillance. Furthermore, perception about the structure of blood vessels may change as further knowledge on the vascular structure is acquired by observing the movement of TMS. This in turn, will affect the trajectory planning in the next round of TMS maneuver. This feedback loop motivates adoption of the cognitive engine as shown in Fig. 4. The engine applies previous measurements of the TMS path ("environment"), and intelligently optimizes the planning of TMS pathway ("control"), in response to the perceived surveillance environment variation such as the structure of the vascular network ("perception") in real time. The feedback loop from the tracking module to the propelling field source ("feedback") facilitate such a learning process. In this way, a visual display of communication channel is provided, which enables the external MAU to control the movement of TMS by "touching" the tangible TMS-maneuvering space with a guiding force.

In general, there are two criteria for TMS path planning. The first criterion aims at minimizing the propagation delay from the injection site to the tumor microenvironment. The second criterion attempts to minimize the attenuation loss of TMS-assisted drug delivery. Depending on the structure of vasculature,

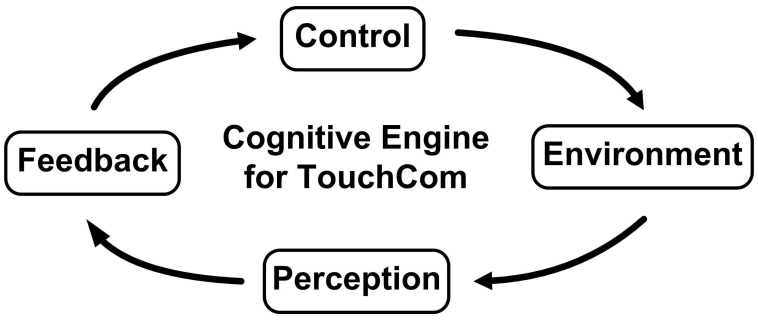

Fig. 4. Cognitive engine for TouchCom.

these two criteria may not always lead to a unique solution. For simplicity, the following heuristic rules for the cognitive engine are proposed in line with the two criteria mentioned above.

1) When blood vessels are resolvable on the angiogram, the control process only occurs at each bifurcation. The cognitive engine chooses the daughter segment that results in the shorter perpendicular distance from the center of the tumor microenvironment to the segment as the traveling path after the bifurcation.
2) When blood vessels are unresolvable on the angiogram, a two-step control is required after the TMS swarm leaves the previous AZ and is about to reach the next AZ. First, the cognitive engine identifies the area with the highest concentration of TMS as the next AZ. Subsequently, the direction of the guiding field is chosen to be aligned with the line connecting the centers of the AZ and the tumor microenvironment.

These two heuristic rules can be readily integrated into the simulation steps mentioned in Section III.

V. Numerical Examples

We present a study case of TouchCom for silicon-based TMS assuming an external propelling field is employed to guide the TMS for targeted drug delivery. We assume that the speed of the TMS swarm is $0.03\ \mathrm{cm/s}$, comparable to the average velocity of blood flow in capillaries. The time spent at each AZ is assumed to be negligible as compared to the propagation time. The injection site is located at the origin. The tumor microenvironment is a circular area centered at $(10\ \mathrm{cm}, 0\ \mathrm{cm})$ and having a radius of $0.5\ \mathrm{cm}$. The diameter and length of the root vessel where the TMS swarm is injected are $0.1\ \mathrm{cm}$ and $1\ \mathrm{cm}$, respectively, and the vessel is aligned with the $x-$axis. The angiographically unresolvable vasculature $\mathrm{V_{ur}}$ is the region defined by $x \geq x_{\mathrm{r}}$, whereas the angiographically resolvable region $\mathrm{V_r}$ is

defined by $x \leq x_{\rm r}$. In the simulation studies, we will consider three different widths of the resolvable region: $x_{\rm r} = 4, 6, 8$ cm.

To synthesize the movement of TMS in $\mathrm{V_r}$, the bifurcation exponent and asymmetric ratio of the vascular tree are set to be uniformly distributed in $[2.6, 2.7]$ and $[0.6, 0.8]$, respectively. The length-to-diameter ratio K is 40. In terms of the movement of TMS in $\mathrm{V_{ur}}$, the following model parameters are used: $\varpi = 0.1$ s^{-1} and $\kappa = 2$. To model the path loss, the degeneration parameters are given by $\Lambda_1 = 20$ min, $\Lambda_2 = 2$ min, and $C^* = 0.5$. We will consider three different diffusion coefficients $D = 10^{-6}, 10^{-7}, 10^{-8}$ m^2/s.

Fig. 5 illustrates a typical path of the TMS swarm when the boundary of angiographically resolvable vasculature and the diffusion coefficient are set to be $x_{\rm r} = 6$ cm and $D = 10^{-7}$ m^2/s, respectively. As can be seen from this figure, the trajectory in $\mathrm{V_r}$ has longer and more regular segments as compared to $\mathrm{V_{ur}}$. Fig. 6 shows the degeneration, diffusion, and overall losses corresponding to the trajectory in Fig. 5. Note that the attenuation caused by diffusion increases abruptly as the TMS swarm enters $\mathrm{V_{ur}}$. On the other hand, the degeneration loss increases gradually throughout the entire transportation process.

The empirical distribution of propagation time from the injection site to the tumor, the pdf of angle-of-arrival at the tumor, and the pdf of path loss for three different values of the diffusion coefficient D are shown in Fig. 7(a)-(c) based on 50000 simulation runs. Furthermore, the delay spectrum and azimuth spectrum are depicted in Fig. 7(d)-(e). As can be seen from Figs. 7(a) and 7(d), both the pdf of delay and delay spectrum first increase with delay and reach their maximum values. Then, the pdfs decrease and exhibit a long tail. The pdfs of time-of-arrival are concentrated within a broader temporal range as compared to the delay spectrum. Furthermore, various D do not lead to noticeable changes in the former plots, whereas a larger D results in smaller delay spreads in the latter plots. Next, the pdf of path loss is featured by a clustering phenomenon as shown in Fig. 7(c). It exhibits a peak at around 0 (i.e., the amount of drug delivered is completely attenuated), together with an asymmetric cluster for larger values of path loss. As D decreases, the chance of successfully delivering more drug molecules increases. Finally, as illustrated in Figs. 7(b) and 7(e), both the pdf of azimuth and azimuth spectrum are symmetric with respect to 0°. The value of D has a negligible effect on the pdf of angle-of-arrival, but has a remarkable effect on the azimuth spectrum.

We then look into the influence of different sizes of the angiographically resolvable region on the distributions. As shown in Fig. 8, all the plots except for the pdf of path loss are insensitive to the change in $x_{\rm r}$. Nevertheless, a larger $x_{\rm r}$ increases the chance of transporting a larger amount of drug cargoes to the tumor microenvironment.

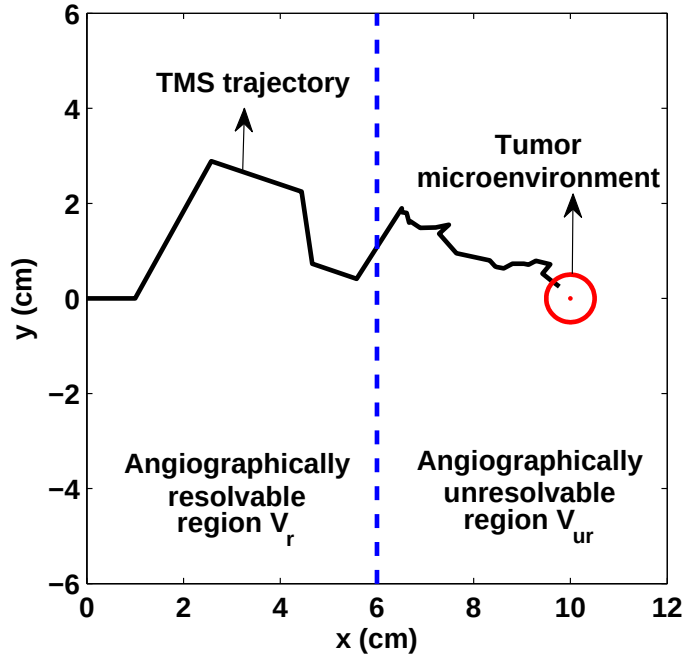

Fig. 5. Simulated TMS trajectory for the diffusion coefficient $D = 10^{-7}$ m^2/s and the boundary of regions $x_\mathrm{r} = 6$ cm.

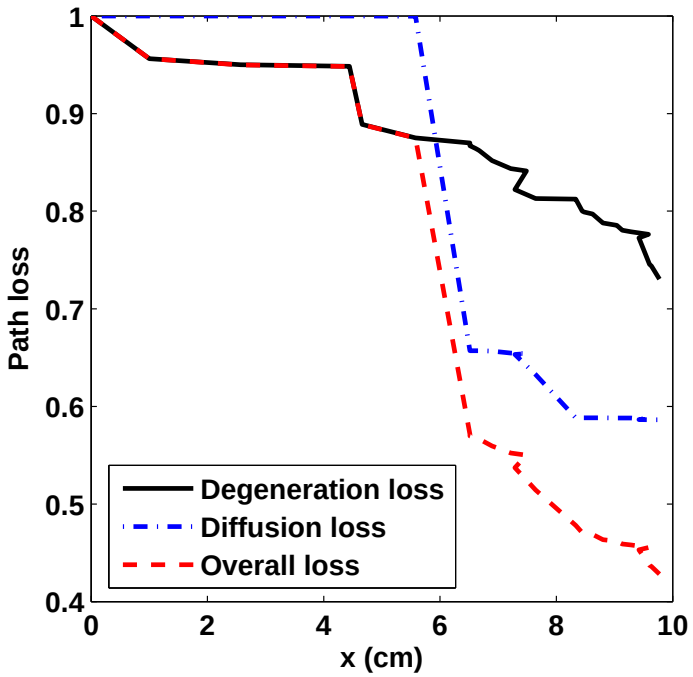

Fig. 6. Path loss for the diffusion coefficient $D = 10^{-7}$ m^2/s and the boundary of regions $x_\mathrm{r} = 6$ cm.

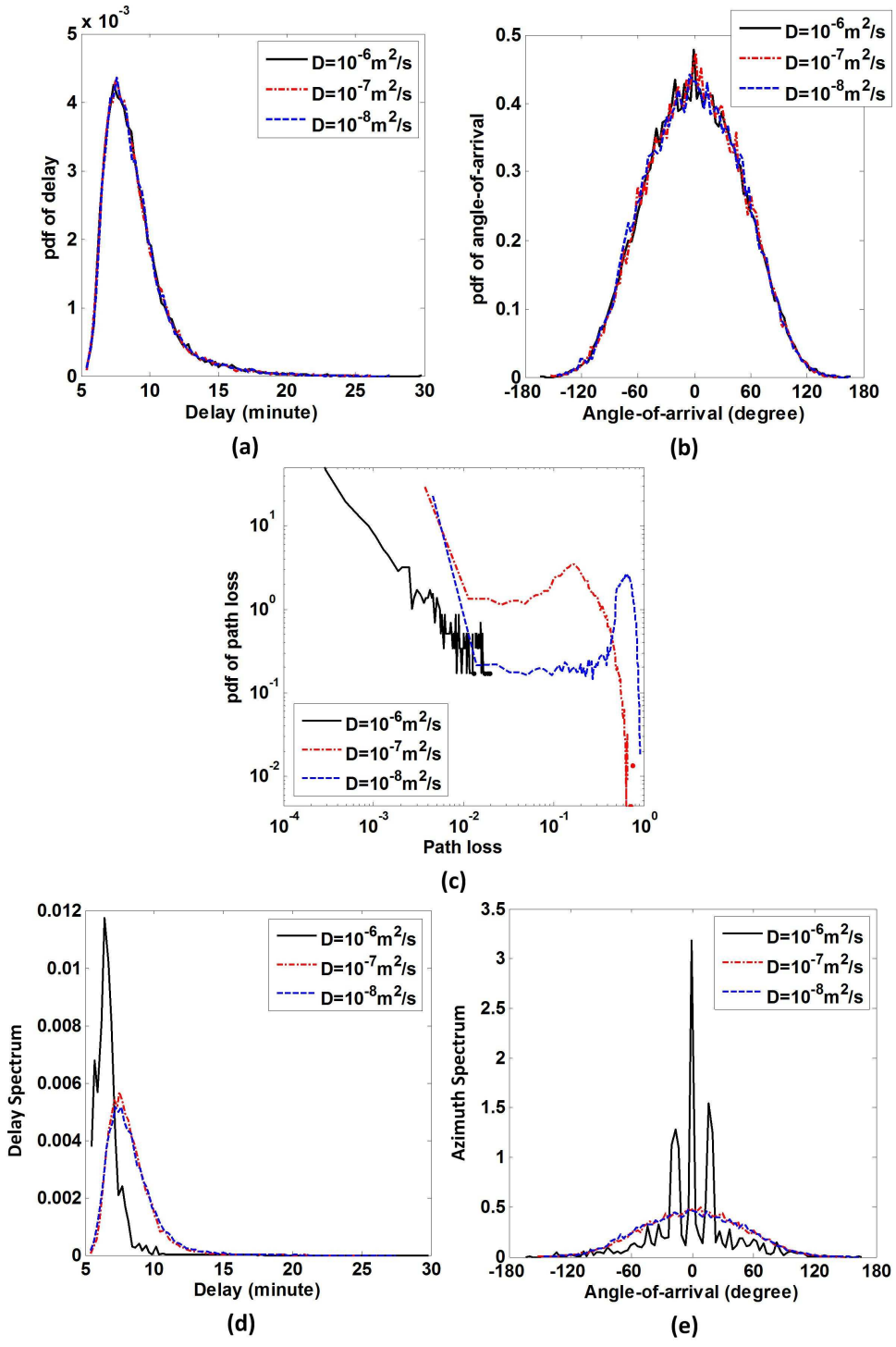

Fig. 7. Pdfs of (a) delay, (b) angle-of-arrival, and (c) path loss; (d) delay spectrum and (e) azimuth spectrum for three different values of diffusion coefficients D. In all cases, the boundary of regions $x_{\mathrm{r}} = 6$ cm.

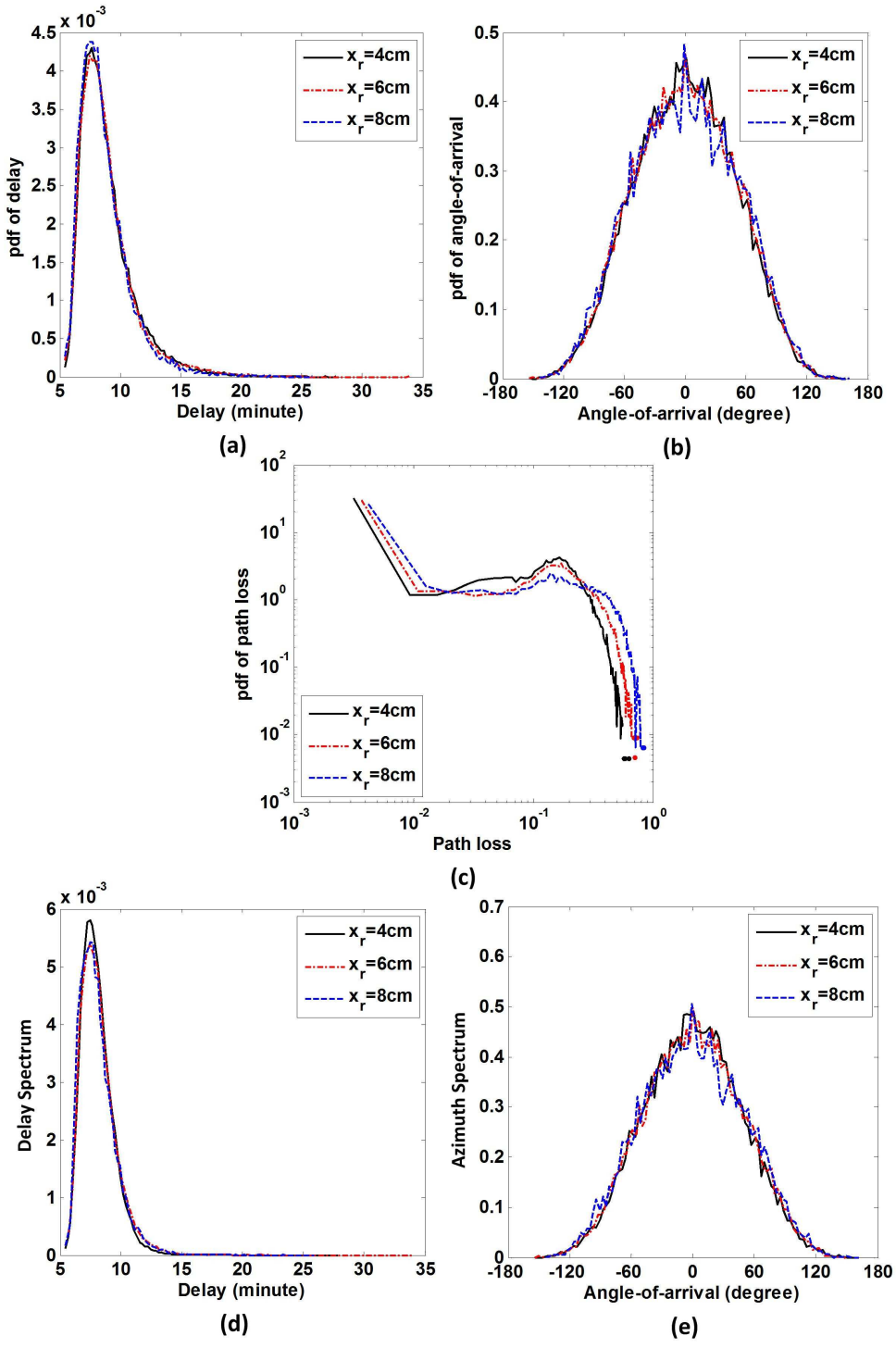

Fig. 8. Pdfs of (a) delay, (b) angle-of-arrival, and (c) path loss; (d) delay spectrum and (e) azimuth spectrum for three different boundaries of angiographically resolvable vasculature x_{r}. In all cases, the diffusion coefficient $D = 10^{-7}\ \mathrm{m}^2/\mathrm{s}$.

VI. Conclusion

We have proposed a TMS-assisted TouchCom model for targeted drug delivery, and analyzed the system architecture and simulation tools of the proposed framework. We have also presented numerical examples to demonstrate the principles of our approach. Specifically, we have investigated the distributions of the delay, angle-of-arrival, and path loss, as well as the delay spectrum and azimuth spectrum, which are important parameters from the perspectives of both drug delivery and information exchange. The TouchCom paradigm represents a unified framework that integrates robotics and communications "at the bottom", and establishes the useful analogy between the TMS-based drug delivery and small-scale communications.

References

[1] R. P. Feynman, "Plenty of Room at the Bottom," 1959, www.its.caltech.edu/ feynman/plenty.html.

[2] S. W. Hwang, X. Huang, J. H. Seo, J. K. Song, S. Kim, S. Hage-Ali, H. J. Chung, H. Tao, F. G. Omenetto, Z. Ma, and J. A. Rogers, "Materials for bioresorbable radio frequency electronics," *Adv. Mater.*, vol. 25, pp. 3526–3531, Jul. 2013.

[3] S. W. Hwang, H. Tao, D. H. Kim, H. Cheng, J. K. Song, E. Rill, M. A. Brenckle, B. Panilaitis, S. M. Won, Y. S. Kim, Y. M. Song, K. J. Yu, A. Ameen, R. Li, Y. Su, M. Yang, D. L. Kaplan, M. R. Zakin, M. J. Slepian, Y. Huang, F. G. Omenetto, and J. A. Rogers, "A physically transient form of silicon electronics," *Science*, vol. 337, pp. 1640–1644, Sep. 2012.

[4] Y. Chen, P. Kosmas, and R. Wang, "Conceptual design and simulations of a nano-communication model for drug delivery based on a transient microbot system," in *Proc. IEEE EuCAP 2014*, Hage, Netherlands, Apr. 2014.

[5] O. M. Koo, I. Rubinstein, and H. Onyuksel, "Role of nanotechnology in targeted drug delivery and imaging: a concise review," *Nanomed.*, vol. 1, no. 3, pp. 193–212, Sep. 2005.

[6] M. Pierobon and I. F. Akyildiz, "Capacity of a diffusion-based molecular communication system with channel memory and molecular noise," *IEEE Trans. Inf. Theory*, vol. 59, pp. 942–954, Feb. 2013.

[7] I. F. Akyildiz, J. M. Jornet, and M. Pierobon, "Nanonetworks: A new frontier in communications," *Commun. ACMs*, vol. 54, pp. 84–89, Nov. 2011.

[8] I. F. Akyildiz, F. Brunetti, and C. Blazquez, "Nanonetworks: A new communication paradigm," *Comput. Netw.*, vol. 52, pp. 2260–2279, Aug. 2008.

[9] T. Nakano, A. W. Eckford, and T. Haraguchi, *Molecular Communications*, Cambridge University Press, 2013.

[10] N. Farsad, A. W. Eckford, S. Hiyama, and Y. Moritani, "On-chip molecular communication: Analysis and design," *IEEE Trans. NanoBiosci.*, vol. 11, pp. 304–314, Sep. 2012.

[11] S. Kadloor, R. S. Adve, and A. W. Eckford, "Molecular communication using Brownian motion with drift," *IEEE Trans. NanoBiosci.*, vol. 11, pp. 89–99, Jun. 2012.

[12] K. V. Srinivas, A. W. Eckford, and R. S. Adve, "Molecular communication in fluid media: The additive inverse Gaussian noise channel," *IEEE Trans. Inf. Theory*, vol. 58, pp. 4678–4692, Jul. 2012.

[13] B. Atakan and O. B. Akan, "Deterministic capacity of information flow in molecular nanonetworks," *Nano Commun. Netw.*, vol. 1, pp. 31–42, Mar. 2010.

[14] B. Atakan and O. B. Akan, "On channel capacity and error compensation in molecular communication," *Trans. Comput. Syst. Biol.*, vol. 10, pp. 59–80, Dec. 2009.

[15] C. Rose and I. Saira Mian, "Signaling with identical tokens: Lower bounds with energy constraints," in *Proc. IEEE ISIT 2013*, Istanbul, Turkey, Jul. 2013.

[16] S. Hiyama and Y. Moritani, "Molecular communications: Harnessing biochemical materials to engineer biomimetic communication systems," *Nano Commun. Netw.*, vol. 1, no. 1, pp. 20–30, 2010.

[17] M. J. Moore, T. Suda, and K. Oiwa, "Molecular communication: Modeling noise effects on information rate," *IEEE Trans. NanoBiosci.*, vol. 8, pp. 169–180, Jun. 2009.

[18] D. Pivonka, A. Yakovlev, A. Poon, and T. Meng, "A mm-sized wireless powered and remotely controlled locomotive implant," *IEEE Trans. Biomed. Circ. Syst.*, vol. 6, pp. 523–532, Dec. 2012.

[19] S. Martel, M. Mohammadi, O. Felfoul, Z. Lu, and P. Pouponneau, "Flagellated magnetotactic bacteria as contralled MRI-trackable propulsion and steering systems for medical nanorobots operating in the human microvasculature," *Int. J. Rob. Res.*, vol. 28, pp. 571–582, Apr. 2009.

[20] S. Martel, O. Felfoul, J.-B. Mathieu, A. Chanu, S. Tamaz, M. Mohammadi, M. Mankewich, and N. Tabatabaei, "MRI-based medical nanorobotic platform for the control of magnetic nanoparticles and flagellated bacteria for target interventions in human capillaries," *Int. J. Rob. Res.*, vol. 28, pp. 1169–1182, Sept. 2009.

[21] S. Martel, O. Felfoul, M. Mohammadi, and J.-B. Mathieu, "Interventional procedure based on nanorobots propelled and steered by flagellated magnetotactic bacteria for direct targeting of tumors in the human body," in *Proc. IEEE EMBC 2008*, Vancouver, Canada, Aug. 2008.

[22] S. Martel, O. Felfoul, and M. Mohammadi, "Flagellated bacterial nanorobots for medical interventions in the human body," in *Proc. IEEE BioRob 2008*, Scottsdale, USA, Oct. 2008.

[23] N. Mokrani, O. Felfoul, F. A. Zarreh, M. Mohammadi, R. Aloyz, G. Batist, and S. Martel, "Magnetotactic bacteria penetration into multicellular tumor spheroids for targeted therapy," in *Proc. IEEE EMBC 2010*, Buenos Aires, Argentina, Sept. 2010.

[24] C. C. Tremblay, J. Jean, L. Marchand, A. Turki, P. Chouinard-Gaouette, M. Brousseau, M. Mohammadi, and S. Martel, "Robotic platform for real-time tracking of a single fast swimming bacterium," in *Proc. IEEE ISOT 2010*, Toronto, Canada, Oct. 2010.

[25] Y. Chen, P. Kosmas, and S. Martel, "Microwave breast tumor detection and size estimation using contrast-agent-loaded magnetotactic bacteria," in *Proc. IEEE EMBC 2013*, Osaka, Japan, Jul. 2013.

[26] Y. Chen, P. Kosmas, and S. Martel, "A feasibility study for microwave breast cancer detection using contrast-agent-loaded bacterial microbots," *Int. J. Antennas Propag.*, vol. 2013, Article ID 309703, 11 pages, http://dx.doi.org/10.1155/2013/309703.

[27] S. P. Sherlock and H. Dai, "Quantum dot bioconjugates for imaging, labeling and sensing," *Nature Materials*, vol. 4, pp. 435–446, 2005.

[28] I. L. Medintz, H. Tetsuo Uyeda, E. R. Goldman, and H. Mattoussi, "Multifunctional FeCo-graphitic carbon nanocrystals for combined imaging, drug delivery and tumor-specific photothermal therapy in mice," *Nano Res.*, vol. 4, pp. 1248–1260, Dec. 2011.

[29] Y. Chen and P. Kosmas, "Detection and localization of tissue malignancy using contrast-enhanced microwave imaging: Exploring information theoretic criteria," *IEEE Trans. Biomed. Eng.*, vol. 59, pp. 766–776, Mar. 2012.

[30] S. Leschka, H. Alkadhi, A. Plass, L. Desbiolles, J. Grünenfelder, B. Marincek, and S. Wildermuth, "Accuracy of MSCT coronary angiography with 64-slice technology: first experience," *Eur. Heart J.*, vol. 26, pp. 1482–1487, Apr. 2005.

[31] M. Zamir, "Fractal dimensions and multifractility in vascular branching," *J. Theor. Biol.*, vol. 212, pp. 183–190, 2001.

[32] E. Gabrys, M. Rybaczuk, and A. Kedzia, "Fractal models of circulatory system. Symmetrical and asymmetrical approach comparison," *Chaos, Solitons & Fractals*, vol. 24, pp. 707–715, May 2005.

[33] K. I. Pedersen, P. E. Mogensen, and B. H. Fleury, "A stochastic model of the temporal and azimuthal dispersion seen at the base station in outdoor propagation environments," *IEEE Trans. Veh. Technol.*, vol. 49, no. 2, pp. 437–447, 2000.

[34] A. F. Molisch, *Wireless Communications*, John Wiley & Sons, Chichester, West Sussex, United Kingdom, 2011.

[35] W. H. Bossert and E. O. Wilson, "The analysis of olfactory communication among animals," *Journal of Theoretical Biology*, vol. 5, pp. 443–469, Nov. 1963.

[36] E. A. Codling, *Biased Random Walks in Biology*, PhD Thesis, The University of Leeds, 2003.

[37] D. J. Best and N. I. Fisher, "Efficient simulation of the von Mises distribution," *Appl. Statist.*, vol. 28, no. 2, pp. 152–157, 1979.